Applied Catalysis B: Environmental 182 (2016) 247–256

Contents lists available at ScienceDirect

Applied Catalysis B: Environmental

journal homepage: www.elsevier.com/locate/apcatb

Photoelectrochemical water oxidation over fibrous and sponge-like $BiVO_4/\beta$-$Bi_4V_2O_{11}$ photoanodes fabricated by spray pyrolysis

Wayler S. dos Santos[a,b], Leandro D. Almeida[c], André S. Afonso[a], Mariandry Rodriguez[a], João P. Mesquita[d], Douglas S. Monteiro[a], Luiz C.A. Oliveira[c], José D. Fabris[b], Márcio C. Pereira[a,*]

[a] Institute of Science, Engineering and Technology, Federal University of the Jequitinhonha and Mucuri Valleys, Teófilo Otoni, Minas Gerais 39803-371, Brazil
[b] Graduate Program in Biofuels, Federal University of the Jequitinhonha and Mucuri Valleys, Campus JK, 39100-000, Diamantina, Minas Gerais, Brazil
[c] Department of Chemistry, Federal University of Minas Gerais, 31270-901 Belo Horizonte, Minas Gerais, Brazil
[d] Federal University of the Jequitinhonha and Mucuri Valleys, Campus JK, 39100-000, Diamantina, Minas Gerais, Brazil

ARTICLE INFO

Article history:
Received 5 July 2015
Received in revised form
11 September 2015
Accepted 15 September 2015
Available online 21 September 2015

Keywords:
Water oxidation
Heterojunction
Semiconductor
Photoanodes

ABSTRACT

Two different heterojunction photoanodes were made by one-pot spray pyrolysis deposition of $BiVO_4/Bi_4V_2O_{11}$ directly onto a conductive FTO substrate or on a previously deposited SnO_2 layer onto an FTO substrate (sample $BiVO_4/Bi_4V_2O_{11}/SnO_2$). The direct deposition onto FTO produced fibrous-like $BiVO_4/Bi_4V_2O_{11}$, whereas the deposition onto SnO_2 gave sponge-like $BiVO_4/Bi_4V_2O_{11}$ morphologies. The photoactivity of these photoelectrodes was investigated for photoelectrochemical water oxidation under visible light irradiation. The fibrous-like $BiVO_4/Bi_4V_2O_{11}$ exhibited higher photoactivity than that of the sponge-like $BiVO_4/Bi_4V_2O_{11}/SnO_2$ film. The transient photocurrent decay studies revealed that the time of e^-/h^+ recombination is higher in fibrous-like $BiVO_4/Bi_4V_2O_{11}$ than sponge-like $BiVO_4/Bi_4V_2O_{11}/SnO_2$ film, which suggests that the electrons might accumulate in the SnO_2 layer, thus causing a higher e^-/h^+ recombination and a lower photoactivity. Electrochemical impedance data showed that the hole transfer from the semiconductor to the water takes place more readily in fibrous-like $BiVO_4/Bi_4V_2O_{11}$ than sponge-like $BiVO_4/Bi_4V_2O_{11}/SnO_2$ films. Consequently, the overall photoelectrochemical cell efficiencies for fibrous-like $BiVO_4/Bi_4V_2O_{11}$ and sponge-like $BiVO_4/Bi_4V_2O_{11}/SnO_2$ films were 0.14 and 0.11%, respectively, without using oxygen evolution catalysts. These photoanodes prepared by spray pyrolysis are thus promising for use in PEC water splitting cells.

1. Introduction

Solar energy storage in chemical bonds offers a sustainable way to solving the energy challenge with minimal impact on the environment. Solar energy conversion can alternatively be carried out in photoelectrochemical cells (PECs), which are devices able to harvest sunlight to drive the water splitting into clean H_2 fuel and O_2 [1]. However, the efficiency of PECs is usually limited by the slow kinetic of water oxidation at the photoanodes, which occurs at significant rates only at high overpotentials. Thus, the challenge to obtain high-efficiency PECs consists in developing or optimizing photoanodes in terms of its semiconductor selection and structure to oxidize water efficiently to O_2 even at low potentials.

Different photoanodes such as TiO_2 [2,3], α-Fe_2O_3 [4,5], WO_3 [6], and $BiVO_4$ [7] have been described in the state of the art of photoelectrochemical water oxidation. It has been predicted that a maximum solar to hydrogen (STH) efficiency at 100 mW cm^{-2} AM 1.5 G global illumination of TiO_2 (rutile, E_g = 3.0 eV), Fe_2O_3 (hematite, E_g = 2.2 eV), WO_3 (E_g = 2.7 eV), and monoclinic $BiVO_4$ (E_g = 2.4 eV) is 2.25% [8], 12.9% [8], 4.8% [8], and 9.2% [9], respectively. The maximum efficiency expected for an ideal semiconductor electrode, with bandgap energy of 2.03 eV, is 16.8% at the same conditions [8]. STH efficiency of 10% has been required to the entrance level of commercialization [10]. Therefore, α-Fe_2O_3 and monoclinic $BiVO_4$ have been reported as the most promising photoanodes for the half-reaction of water oxidation. Despite its high theoretical STH efficiency, the photoelectrochemical activity of hematite is limited by its relatively poor absorptivity, very short excited-state ($\sim 10^{-12}$ s), poor oxygen evolution reaction kinetic, and short hole diffusion length [4]. Alternatively, n-type monoclinic $BiVO_4$ with a direct bandgap of 2.4 eV [11], allowing it to absorb

* Corresponding author. Fax: +55 33 3522 6037.
E-mail address: mcpqui@gmail.com (M.C. Pereira).

http://dx.doi.org/10.1016/j.apcatb.2015.09.034
0926-3373/

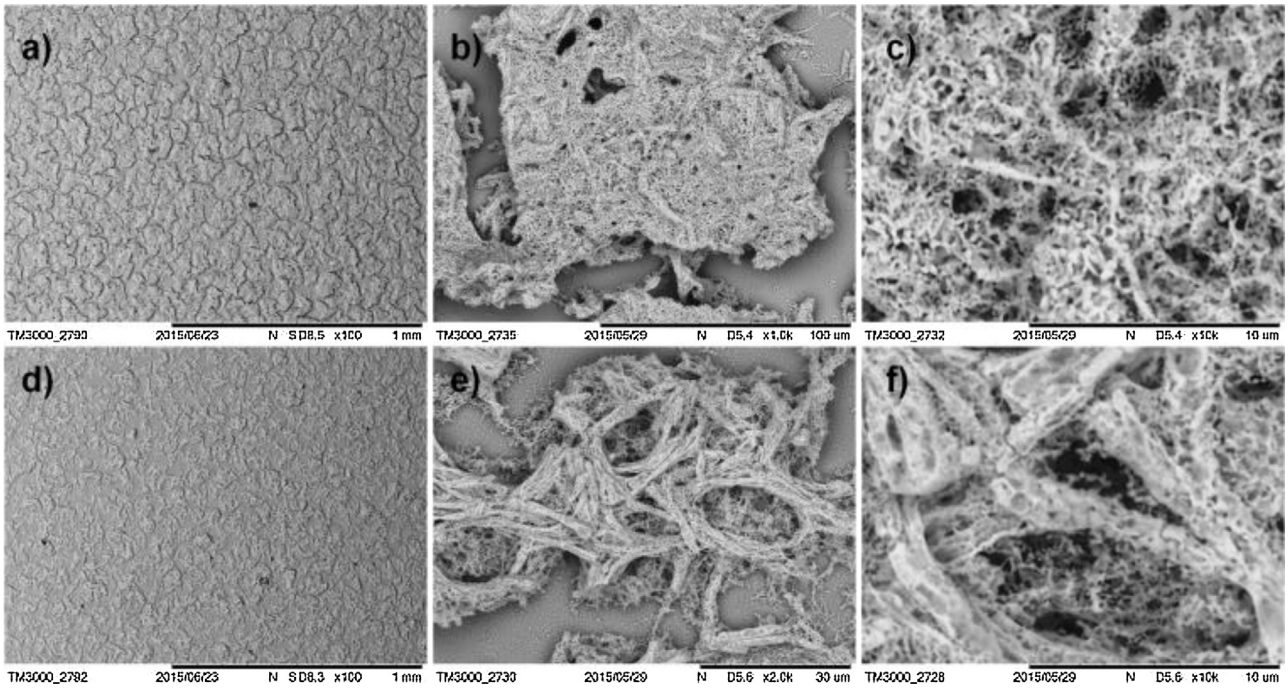

Fig. 1. SEM images obtained for (a–c) sponge-like $BiVO_4/Bi_4V_2O_{11}/SnO_2$, and (d–f) fibrous-like $BiVO_4/Bi_4V_2O_{11}$ films deposited on FTO substrates.

approximately 11% of the solar spectrum, is one of the most active photoanodes for the water oxidation. Assuming a Faradaic efficiency of 100% in $BiVO_4$, theoretical photocurrents of ~7.5 mA cm^{-2} at 1.23 V_{RHE} (volts vs. a reversible hydrogen electrode) could be achieved under AM 1.5 G irradiation [12]. Nevertheless, the practical STH efficiency of $BiVO_4$ is still low (e.g. <1%), as it suffers from excessive electron-hole recombination, poor charge transport properties, and poor water oxidation kinetics [7]. Therefore, the development of photoanodes for water oxidation still really is a challengeable task to materials researchers.

The heterojunction or heterostructure concept is an excellent alternative to designing materials with improved photocatalytic properties [13]. The combination of two semiconductors has been reported to change the electronic structure of the interface between the semiconductors, thus increasing the light absorption, enhancing the charge separation, and increasing the kinetic of the reactions [14].

Recently, a layered perovskite-type β-orthorhombic $Bi_4V_2O_{11}$ belonging to the Aurivillius family was reported to exhibit an anodic photocurrent density of 4.77 μA cm^{-2} at 1 V vs. Ag/AgCl due to the water oxidation in the presence of methanol, under UV–vis irradiation [15]. $Bi_4V_2O_{11}$ is an n-type semiconductor with a bandgap energy of 2.25 eV, and the energy level of the valence (E_{VB}) and conduction (E_{CB}) bands of 2.78 and 0.53 eV vs. RHE, respectively [16]. It makes this perovskite suitable to be coupled with $BiVO_4$, as its conduction band level (0.02 – 0.2 V vs. RHE) [17] is more negative than the E_{CB} of $Bi_4V_2O_{11}$. Hence, excited electrons can be injected from the E_{CB} of $BiVO_4$ to the E_{CB} of the $Bi_4V_2O_{11}$ under visible light irradiation, improving the charge separation on the semiconductors.

With this in mind, we fabricated a fibrous and a sponge-like heterojunction photoanode by combining monoclinic $BiVO_4$ and orthorhombic $Bi_4V_2O_{11}$ in an one-pot spray pyrolysis synthesis for

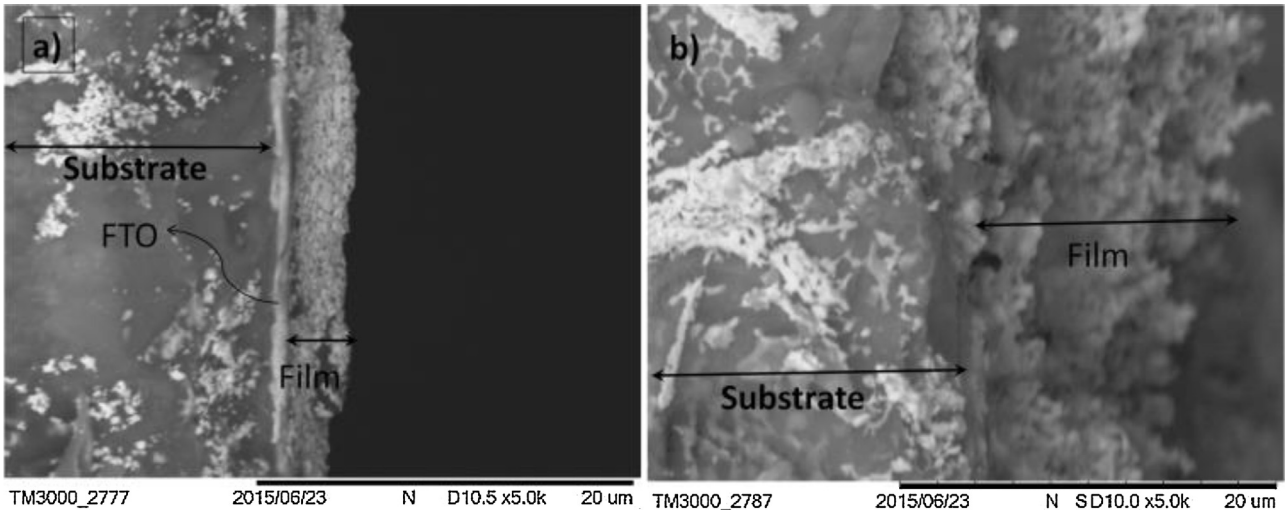

Fig. 2. Thickness characterization of the (a) fibrous-like $BiVO_4/Bi_4V_2O_{11}$, and (b) sponge-like $BiVO_4/Bi_4V_2O_{11}/SnO_2$ films. The arrows indicate different materials.

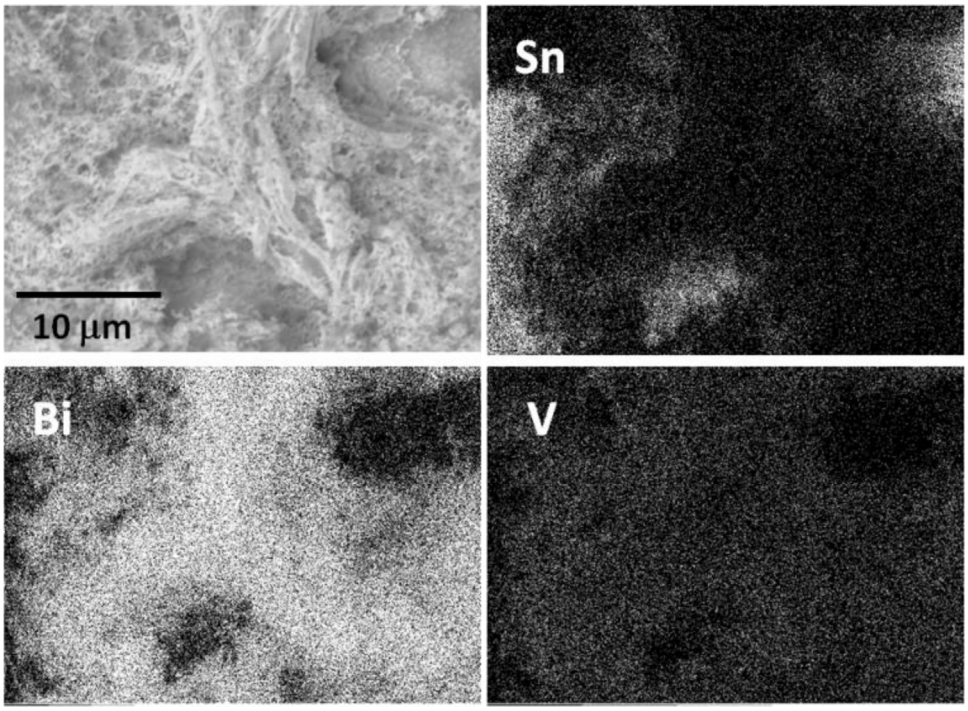

Fig. 3. EDS mapping results conducted on the fibrous-like $BiVO_4/Bi_4V_2O_{11}$ film deposited on FTO substrates.

the photoelectrochemical water oxidation reaction under visible light ($\lambda > 450$ nm), without using oxygen evolution catalysts.

2. Experimental

2.1. Solution preparation for the synthesis of the photoanodes

All chemicals were used as received without further purification. Ten millimoles of ammonium metavanadate (NH_4VO_3, 99%) were dissolved in 50 mL of 174.2 mmol NH_4OH (24.5%) to obtain the solution "A". In another recipient, 10 mmol of $Bi(NO_3)_3{\cdot}5H_2O$ was dissolved in 50 mL of 174.2 mmol CH_3COOH (99.7%), producing the solution "B". Both the solutions were maintained separately under magnetic stirring at 80 °C to obtain stable and homogeneous solutions. Then, the solutions A and B were mixed under stirring at 80 °C for 90 min. Subsequently, 40 mmol citric acid was added to the mixture, and the resultant solution was kept standing for five days. The solution was then diluted with 100 mL deionized water

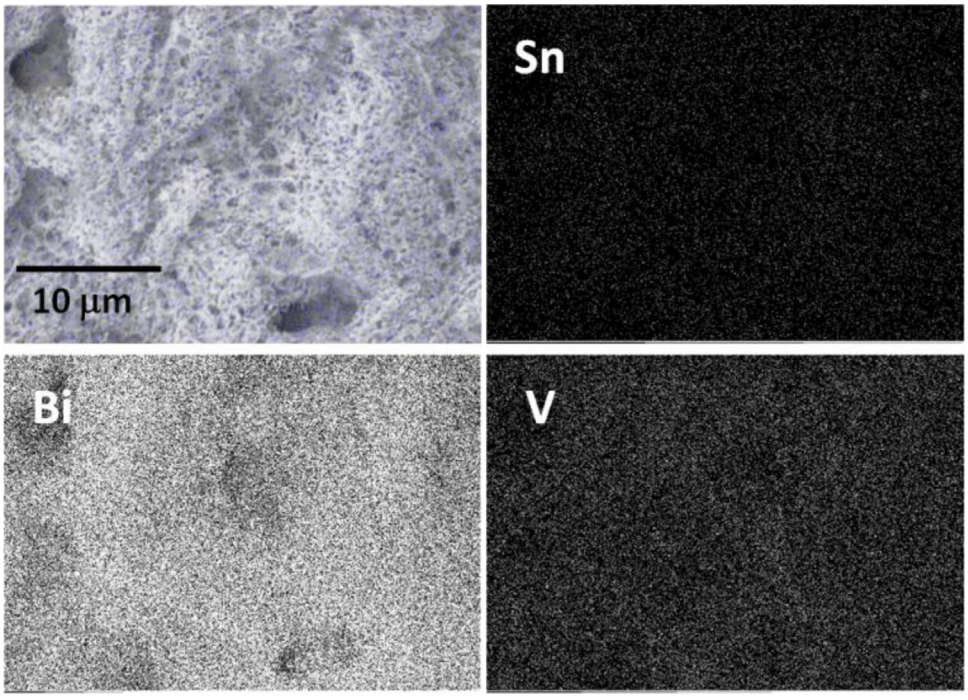

Fig. 4. EDS mapping results conducted on the sponge-like $BiVO_4/Bi_4V_2O_{11}/SnO_2$ film deposited on FTO substrates.

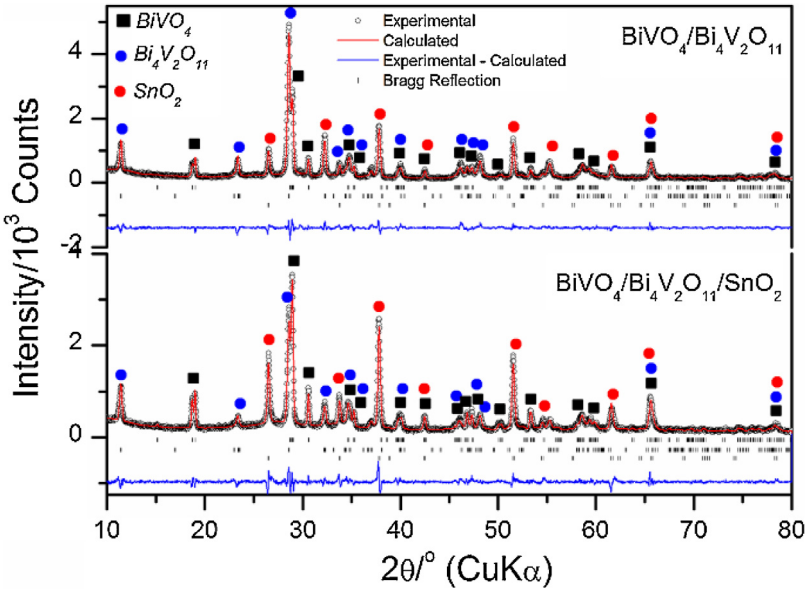

Fig. 5. Rietveld refinement of the XRD patterns of fibrous-like $BiVO_4/Bi_4V_2O_{11}$, and sponge-like $BiVO_4/Bi_4V_2O_{11}/SnO_2$ films deposited on FTO substrates.

and heated at 80 °C until the solution became light blue. This completely dissolved solution was used as a precursor to coat the FTO glass substrates.

2.2. Preparation of the photoanodes

Transparent conductive FTO-coated glass (10 mm × 30 mm × 2 mm, 16 Ω cm^{-2}) were used as substrates for the deposition of the films. Before deposition of semiconductors onto FTO, the substrate surface was cleaned in an ultrasonic bath using acetone and ethanol each for 15 min. After the cleaning procedure, the substrates were dried in a furnace at 120 °C for 1 h. The resultant precursor solution was sprayed down using a commercial airbrush (0.3 mm nozzle) directly onto the FTO glass at a temperature of 300 °C at a distance of 20 cm. 1 cycle of spray with 5 s time deposition were used. Films were subsequently annealed in air in a muffle furnace at 500 °C for 5 h. This sample was named $BiVO_4/Bi_4V_2O_{11}$.

A second photoanode was prepared as described above, except by the previous deposition of an alcoholic solution of $SnCl_2{\cdot}2H_2O$ onto FTO. Briefly, 0.4513 g $SnCl_2{\cdot}2H_2O$ was dissolved in 50 mL ethanol (99.8%) and 2 drops of CH_3COOH (99.7%). The spray deposition was performed at 300 °C at a distance of 20 cm, with 2 cycles of spray deposition for 5 s each cycle. Films were subsequently annealed in air in a muffle furnace at 450 °C for 2 h, to produce a SnO_2 layer (6500 Ω cm^{-2}). Finally, the $BiVO_4/Bi_4V_2O_{11}$ was deposited using the same procedure for the deposition of $BiVO_4/Bi_4V_2O_{11}$ without the SnO_2 layer, and the resultant film heated at 500 °C for 5 h. This sample was named $BiVO_4/Bi_4V_2O_{11}/SnO_2$.

2.3. Characterization of the photoanodes

The morphology of films was investigated by scanning electron microscopy (SEM) using a tabletop SEM (Hitachi TM – 300). EDS mapping were obtained in a SwiftED3000 (Oxford Instruments) at

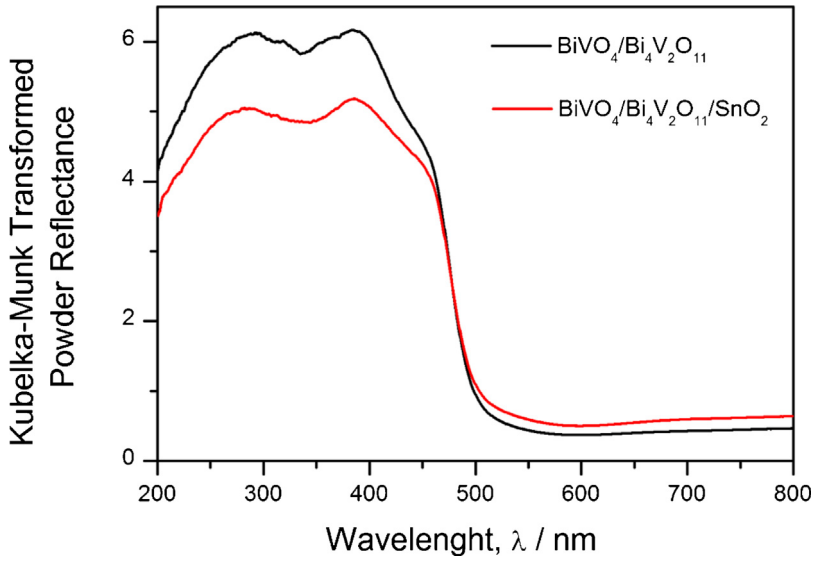

Fig. 6. UV–vis diffuse reflectance spectra of the fibrous-like $BiVO_4/Bi_4V_2O_{11}$ and sponge-like $BiVO_4/Bi_4V_2O_{11}/SnO_2$ films deposited on FTO substrates.

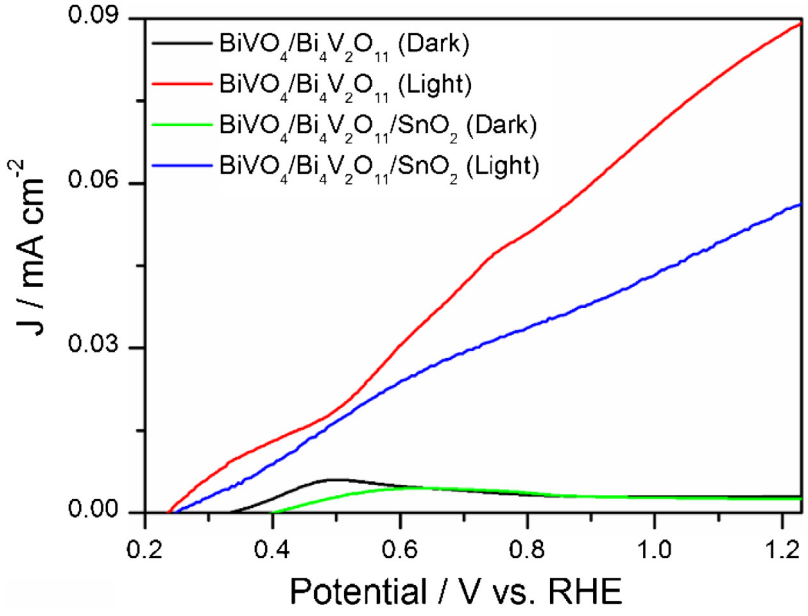

Fig. 7. Cyclic voltammetry sweeps in 0.5 M Na_2SO_4 in the dark and under white light LED for fibrous-like $BiVO_4/Bi_4V_2O_{11}$ and sponge-like $BiVO_4/Bi_4V_2O_{11}/SnO_2$ films deposited on FTO substrates.

15 kV accelerating voltage. The crystalline phases of the films were determined using an X-ray diffractometer (XRD 6000, Shimadzu). The data were collected from 10 to 80° 2θ at a step width of 0.2°, 10 s per step, at 40 kV, 200 mA, and CuKα radiation (λ = 1.540560 Å). Silicon was used as an external standard. The Rietveld structural refinement was performed with FullProf_Suite 2015 software. The diffuse reflectance spectra were collected with a UV–vis spectrometer (Shimadzu UV 2700). Teflon powder was used as reference material (100% transmission), and the Kubelka–Munk equation was used to manipulate all data.

2.4. Photoelectrochemical measurements

The photoelectrochemical measurements were carried out with a potentiostat (AUTOLAB Potentiostat-Galvanostat PGSTAT 128N) using a standard three-electrode cell with an Ag/AgCl (3.0 M KCl) reference electrode, a platinum wire as a counter electrode, a working electrode with irradiation area of 1.0 cm^2, and scan rate of 50 mV s^{-1}. A 0.5 M Na_2SO_4 aqueous solution was used as electrolyte. The prepared films were connected to a copper tape to measure the photoactivity. The photocurrent-potential curves were recorded under a white light LED (light intensity of 0.55 mW cm^{-2}, λ > 450 nm). For converting the obtained potential (vs. Ag/AgCl) to RHE, the following equation was used:

$$E_{RHE} = E_{Ag/AgCl} + 0.059 \times pH + E^{\circ}_{Ag/AgCl}$$

$$E^{\circ}_{Ag/AgCl}(3.0\,M\,KCl) = 0.197\,V\,at\,25\,^{\circ}C$$

The electrochemical impedance spectroscopy (EIS) was performed using an AUTOLAB Potentiostat-Galvanostat PGSTAT 128N

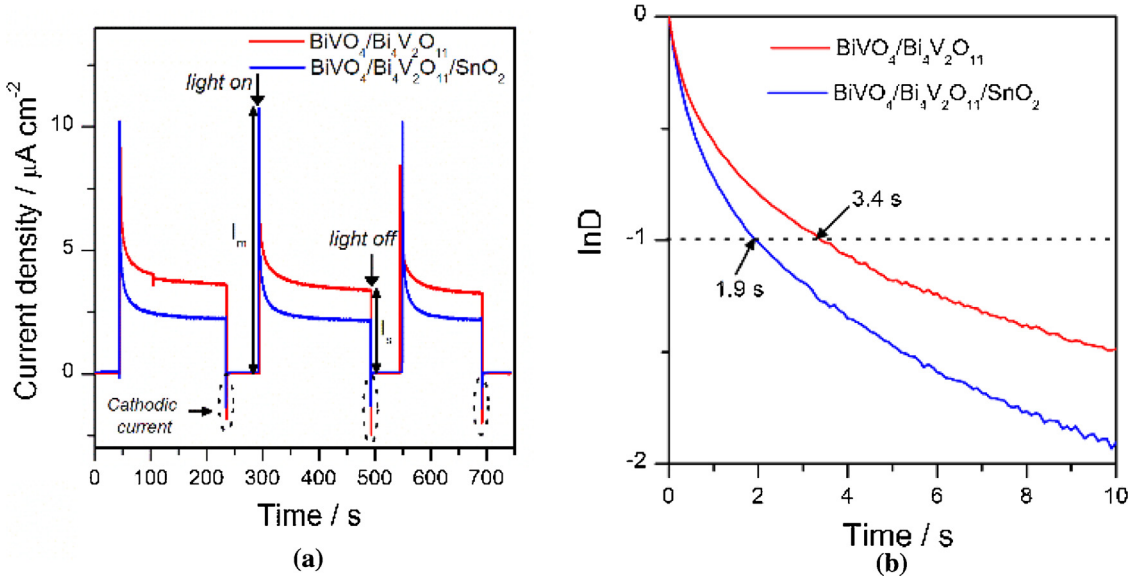

Fig. 8. (a) Transient photocurrent decay that occurs immediately upon illumination at an applied potential of 1.23 V vs. RHE. (b) Transient decay times of fibrous-like $BiVO_4/Bi_4V_2O_{11}$ and sponge-like $BiVO_4/Bi_4V_2O_{11}/SnO_2$ films deposited on FTO substrates.

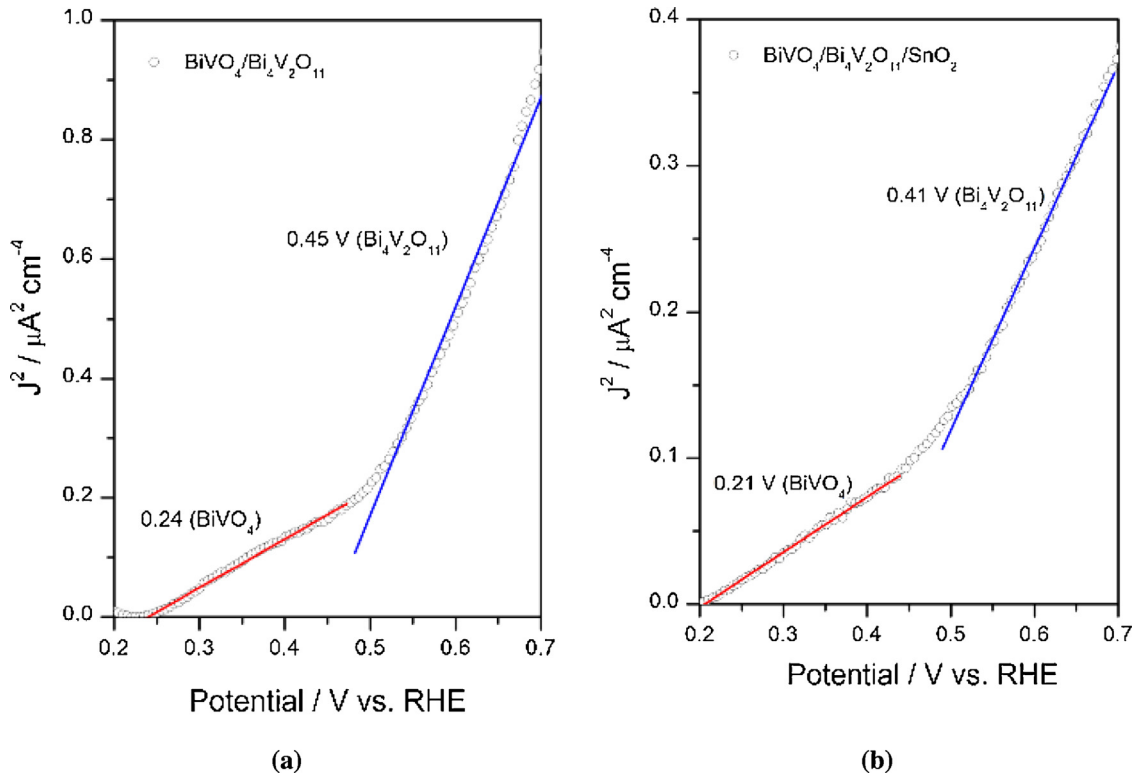

Fig. 9. Onset potential determination from (current density)^2 versus the applied potential dependence for (a) fibrous-like $BiVO_4/Bi_4V_2O_{11}$, and (b) sponge-like $BiVO_4/Bi_4V_2O_{11}/SnO_2$ films deposited on FTO substrates. Light source = white LED, light intensity = 0.55 mW cm^{-2}, 0.5 M Na_2SO_4 electrolyte in the presence of 0.05 M methanol solution.

equipped with the FRA32 M module. The Nyquist plots were measured at 0.7 V (vs. Ag/AgCl) with an AC amplitude of 20 mV, frequency of 100 kHz–100 mHz under a white light LED (light intensity of 0.55 mW cm^{-2}, $\lambda > 450$ nm). The measured spectra were fitted using the NOVA 1.11 software. The 0.5 M Na_2SO_4 solution was used for the all electrochemical measurements.

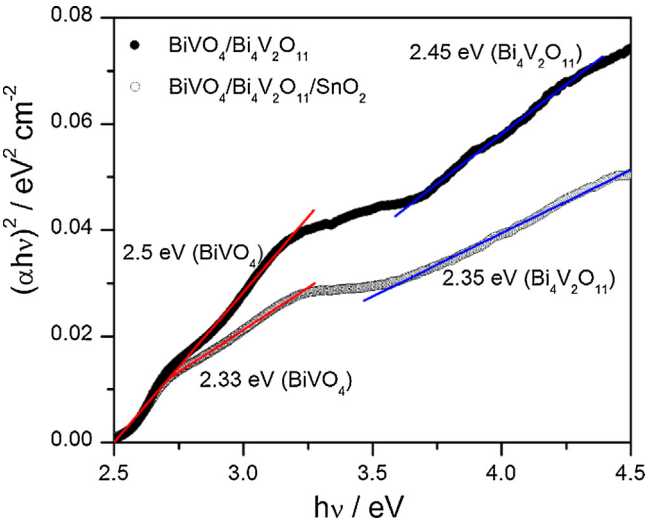

Fig. 10. Tauc plot of fibrous-like $BiVO_4/Bi_4V_2O_{11}$ and sponge-like $BiVO_4/Bi_4V_2O_{11}/SnO_2$ films deposited on FTO substrates.

3. Results and discussion

3.1. Characterization of the photoanodes

The dispersion of the $BiVO_4/Bi_4V_2O_{11}$ and $BiVO_4/Bi_4V_2O_{11}/SnO_2$ particles over the FTO substrate surface was studied by SEM. In general, SEM images showed that the oxides are well-dispersed, covering the whole surface of the FTO (Fig. 1a and d). It was observed that in most of the substrate surface of $BiVO_4/Bi_4V_2O_{11}$ films the formation of islands of a macroporous fibrous-like texture (Fig. 1e and f). On the other hand, the $BiVO_4/Bi_4V_2O_{11}/SnO_2$ film displayed a highly porous sponge-like structure that are formed by sub-micrometer particles (Fig. 1b and c). Both morphologies might have a relatively high area, thus contributing to the substantial photocatalytic activity of the films. Due to the highly porous texture, the films obtained here have the traditional advantages of the supported photocatalyst combined with a higher efficiency in light absorption due to the greater incidence of light through the coupled photocatalyst and the facility of water and gases diffusion throughout the porous structure.

Thickness characterization of the spray pyrolysis films was also made using SEM analysis. Fig. 2a and b shows the thickness characterization of the films grown on an FTO substrate. The images were taken from different regions of the film, and Fig. 2 is a close-up of the lateral view of the film. SEM characterization revealed the thickness of ~3 μm for the fibrous-like $BiVO_4/Bi_4V_2O_{11}$. Moreover, the sponge-like $BiVO_4/Bi_4V_2O_{11}/SnO_2$ film presented a thickness of approximately 15 μm.

EDS mapping (Figs. 3 and 4) of the fibrous-like $BiVO_4/Bi_4V_2O_{11}$ and sponge-like $BiVO_4/Bi_4V_2O_{11}/SnO_2$ films showed the presence of Bi and V throughout the FTO surface. It is interesting to observe

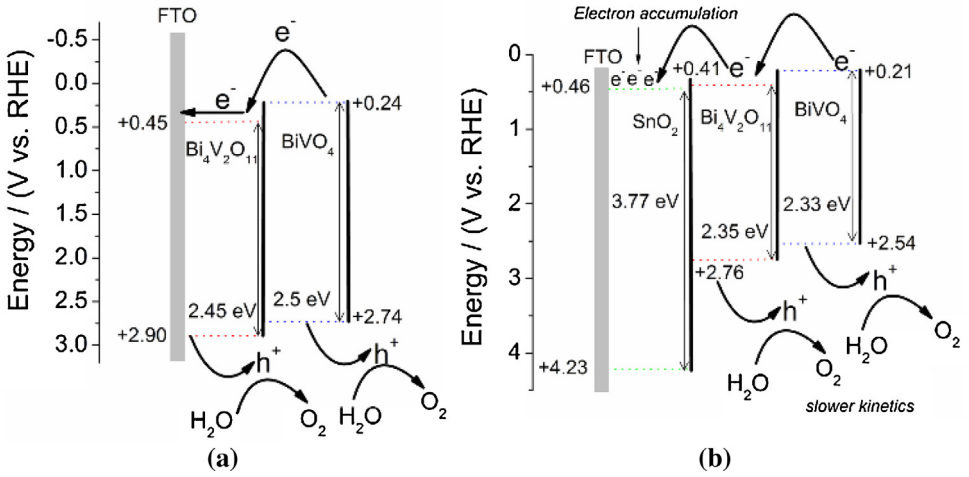

Fig. 11. Schematics of the potential energy diagram for the $BiVO_4/Bi_4V_2O_{11}$ and $BiVO_4/Bi_4V_2O_{11}/SnO_2$ films deposited on FTO substrates.

that Bi and V mapping suggests the presence of these metals throughout the substrate surface, as suggested by the SEM images (Fig. 1). The presence of tin substrate can be clearly seen in the Sn mapping (Figs. 3 and 4).

XRD analyses (Fig. 5) were performed to identify the crystallographic phases present in the films. The qualitative analyses of the XRD patterns of films indicated that both the samples are constituted of $BiVO_4$ (JCPDS—14688) and $Bi_4V_2O_{11}$ (JCPDS—42-349). In addition to these phases, both the samples exhibited reflections due to the conductive FTO substrate. The intensities of these reflections were higher in the $BiVO_4/Bi_4V_2O_{11}/SnO_2$ film, due to the previously deposited SnO_2 (JCPDS—46-1088) onto FTO substrate. The subsequent Rietveld refinement of the XRD data (Fig. 5) with pseudo-Voigt peak fitting gave the structural parameters for the phase present in all samples. The Rietveld refinement yielded a residual profile factor, S, of 1.6 for each film, indicative of good quality refinement models. The XRD pattern of $BiVO_4/Bi_4V_2O_{11}$ film was indexed with a monoclinic (space group *I112/b*) $BiVO_4$ lattice with parameters ($a = 5.1809(3)$, $b = 5.0918(3)$, $c = 11.6807(5)$ Å, and $\gamma = 90.293(5)$), and an orthorhombic (Amam) $Bi_4V_2O_{11}$ lattice ($a = 5.5493(6)$, $b = 5.5526(5)$, $c = 15.4676(8)$ Å). Rietveld refinement of the $BiVO_4/Bi_4V_2O_{11}/SnO_2$ film displayed a $BiVO_4$ unit cell with parameters ($a = 5.1817(2)$, $b = 5.0918(2)$, $c = 11.6812(4)$ Å, $\gamma = 90.290(3)$), $Bi_4V_2O_{11}$ ($a = 5.5484(4)$, $b = 5.5575(9)$, $c = 15.4642(9)$ Å), and SnO_2 ($a = 4.7608(1)$, $c = 3.1983(2)$ Å).

The optical behavior of the films was studied by UV–vis spectroscopy as shown in Fig. 6. The light absorption of the films started at around 510 nm in correspondence with the bandgap energy of its components. It shows that the heterojunctions can be activated by sunlight, which is attractive for application in processes of solar power storage.

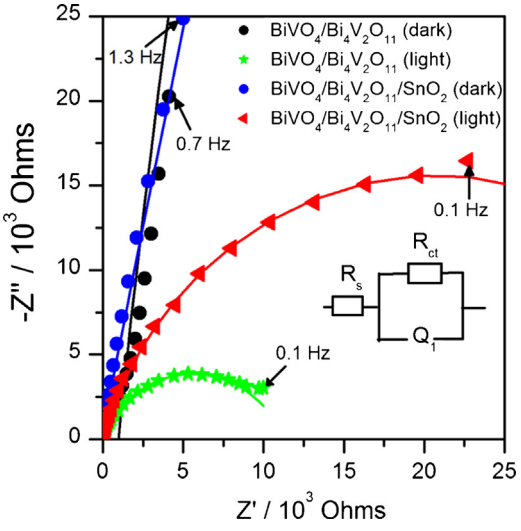

Fig. 12. Electrochemical impedance spectra of fibrous-like $BiVO_4/Bi_4V_2O_{11}$ and sponge-like $BiVO_4/Bi_4V_2O_{11}/SnO_2$ films deposited on FTO substrates.

3.2. Photoelectrochemical measurements

The photoactivity of each film was determined by measuring the photocurrent density generated during water oxidation as white light LED (light intensity: 0.55 mW cm^{-2}) was irradiated on the photoanodes immersed in 0.5 M Na_2SO_4 (at pH 6.6). Both the photoanodes were stable in aqueous solution at this pH. Fig. 7 displays the photocurrent density curves of the fibrous-like $BiVO_4/Bi_4V_2O_{11}$ and sponge-like $BiVO_4/Bi_4V_2O_{11}/SnO_2$ films in the dark and under light irradiation. The dark current density was under 0.002 mA cm^{-2} at 1.23 V vs. RHE in all cases. Under light irradiation, the photocurrents increased with increasing applied anodic potential indicating a typical n-type semiconductor behavior because both $BiVO_4$ and $Bi_4V_2O_{11}$ are n-type semiconductors [7,15]. The photocurrent density of $BiVO_4/Bi_4V_2O_{11}$ and $BiVO_4/Bi_4V_2O_{11}/SnO_2$ photoanodes was 0.090 and 0.055 mA cm^{-2} at 1.23 V vs. RHE, respectively, which indicates that the fibrous-like $BiVO_4/Bi_4V_2O_{11}$ film was approximately 1.6 times more photoactive than the sponge-like $BiVO_4/Bi_4V_2O_{11}/SnO_2$ electrode.

The transient photocurrent decay (Fig. 8a) occurring immediately upon illumination was evaluated to obtain a qualitative understanding of the charge recombination behavior in the prepared photoanodes. When the light was switched on, a photocurrent spike was observed at an applied potential of 1.23 V vs. RHE due to the rapid generation of electron(e^-)/holes (h^+) pairs, which quickly recombined after generation. Therefore, the current decay can be assigned to e^-/h^+ recombination processes, which cause a decreasing in the photoactivity of the film for the water oxidation reaction. Charge recombination can be caused by either accumulation of electrons in the bulk or accumulation of holes at the surface [18]. The accumulation of holes would cause an equally large cathodic transient when the light is switched off, and electrons in the conduction band react with the accumulated holes [19]. However, cathodic transients can scarcely be observed in Fig. 8b, suggesting the accumulation of holes at the surface of

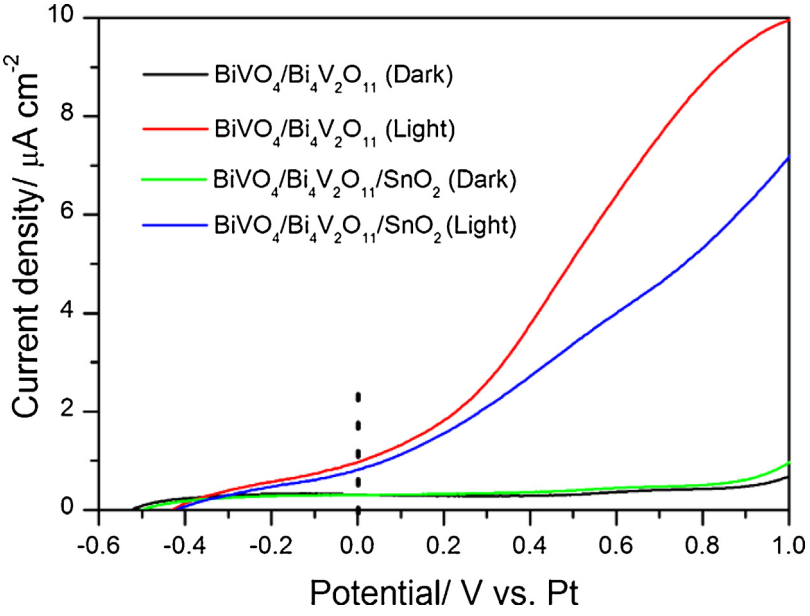

Fig. 13. Cyclic voltammetry sweeps in 0.5 M Na_2SO_4 in the dark and under white light LED for $BiVO_4/Bi_4V_2O_{11}$ and $BiVO_4/Bi_4V_2O_{11}/SnO_2$ films deposited on FTO substrates.

films not be the main recombination process in $BiVO_4/Bi_4V_2O_{11}$ and $BiVO_4/Bi_4V_2O_{11}/SnO_2$ films. Thus, the transients in Fig. 8b were attributed to the accumulation of electrons due to the poor electron carriage in the photoanodes. The transient decay time in the photoanodes was calculated from a logarithmic plot of parameter D, given by the equation [20]:

$$D = \frac{(I_t - I_s)}{(I_m - I_s)}$$

Where I_m is the photocurrent spike, I_t is the photocurrent at time t and I_s is the steady state photocurrent (i.e. as the recombination and charge generation reaches equilibrium) [20]. The transient decay time is defined as the time at which $\ln D = -1$ [21]. Based on the photocurrent profiles measured in Fig. 8a, the transient decay times of $BiVO_4/Bi_4V_2O_{11}$ and $BiVO_4/Bi_4V_2O_{11}/SnO_2$ photoanodes were calculated and plotted in Fig. 8b. The transient decay time for the fibrous-like $BiVO_4/Bi_4V_2O_{11}$ film was 3.4 s, which is approximately 1.8 times longer than the transient decay time of sponge-like $BiVO_4/Bi_4V_2O_{11}/SnO_2$ films (1.9 s). The photocurrent decay rate is determined by the degree to which recombination dominates the charge generation process [20]. Thus, a slower recombination rate would lead to longer transient decay times. Hence, we suggest that the recombination rate was lower in the fibrous-like $BiVO_4/Bi_4V_2O_{11}$ than in the sponge-like $BiVO_4/Bi_4V_2O_{11}/SnO_2$ films.

3.3. Mechanism of charge transfers on the photoanodes

To understand the origin of the highest photocurrent exhibited by the $BiVO_4/Bi_4V_2O_{11}$, it useful to determine the potential energy diagram of the photoanodes. To determine the relative band positions of each component in the heterojunction, we measured flat band potentials and optical band gaps of $BiVO_4$ and $Bi_4V_2O_{11}$.

The flat band potential was measured by the photocurrent onset potential of the photoanodes in 0.5 M Na_2SO_4 electrolyte with 0.05 M methanol solution (Fig 9a and b). The methanol can bring down the kinetic barrier for charge transport by capturing the photogenerated hole efficiently, thus minimizing the errors in the flat band determination [22]. Fig. 9a and b show (current density)^2 – potential [23] dependence of $BiVO_4/Bi_4V_2O_{11}$ and $BiVO_4/Bi_4V_2O_{11}/SnO_2$ films. The straight lines (Fig. 9a) were observed with the intercept at 0.24 ± 0.01 and 0.45 ± 0.02 V vs. RHE, which correspond to the flat band potential of $BiVO_4$ and $Bi_4V_2O_{11}$ respectively in the $BiVO_4/Bi_4V_2O_{11}$ film. For the $BiVO_4/Bi_4V_2O_{11}/SnO_2$ film, the calculated flat band potentials (Fig. 9b) for $BiVO_4$ and $Bi_4V_2O_{11}$ were 0.21 ± 0.01 and 0.41 ± 0.01 V vs. RHE. These calculated values are in agreement with those reported in the literature [16,17]. Assuming the gap between flat band potential and bottom edge of the conduction band is negligible for n-type semiconductors [24], these values reflect the conduction band level of $BiVO_4$ and $Bi_4V_2O_{11}$ at pH 6.6.

To calculate valence band position, the band gap energies of $BiVO_4$ and $Bi_4V_2O_{11}$ were calculated by the following Tauc equation [25]:

$$(\alpha h\nu)^n = A(h\nu - E_g)$$

where A = constant, $h\nu$ = light energy, E_g = optical band gap energy, α = measured absorption coefficient, $n = 2$ for direct band gap. In Fig. 10, the extrapolation of the Tauc plot on x-intercepts gave the optical band gaps of 2.50 and 2.33 eV for $BiVO_4$ in $BiVO_4/Bi_4V_2O_{11}$ and $BiVO_4/Bi_4V_2O_{11}/SnO_2$ films, respectively, whereas for the $Bi_4V_2O_{11}$ the calculated band gaps were 2.45 and 2.35 eV, respectively in fibrous-like $BiVO_4/Bi_4V_2O_{11}$ and sponge-like $BiVO_4/Bi_4V_2O_{11}/SnO_2$ films.

Based on these estimated values of flat band potentials and optical band gap energies, we estimated the valence band energy and built the potential energy diagram for the photoanodes (Fig. 11a and b). For the $BiVO_4/Bi_4V_2O_{11}$ film, the calculated valence band energies for $BiVO_4$ and $Bi_4V_2O_{11}$ were 2.50 ± 0.03 and 2.45 ± 0.05 V vs. RHE, respectively, whereas for the $BiVO_4/Bi_4V_2O_{11}/SnO_2$ film the valence band energy was 2.33 ± 0.05 for $BiVO_4$ and 2.35 ± 0.06 V vs. RHE for $Bi_4V_2O_{11}$. The conduction band of $BiVO_4$ is more negative than the corresponding band of $Bi_4V_2O_{11}$. This thermodynamic status favors the injection of photogenerated electrons from the conduction band of $BiVO_4$ to that of $Bi_4V_2O_{11}$. Therefore, when the $BiVO_4/Bi_4V_2O_{11}$ photoanode is irradiated with white light, excited electrons are generated in the conduction band of both $BiVO_4$ and $Bi_4V_2O_{11}$. The photogenerated electrons in $BiVO_4$ move to the conduction band of $Bi_4V_2O_{11}$ due to the potential difference, and then the excited and migrated electrons in $Bi_4V_2O_{11}$ are collected onto conductive FTO. Otherwise, the holes migrate to the semiconductor/electrolyte interface either directly or after

transfer from $Bi_4V_2O_{11}$ to $BiVO_4$ to oxidize water to O_2. Upon the previous SnO_2 deposition onto FTO, the photoactivity of the sponge-like $BiVO_4/Bi_4V_2O_{11}/SnO_2$ film decreased compared with fibrous-like $BiVO_4/Bi_4V_2O_{11}$, suggesting that the electron transfer from the SnO_2 to the FTO substrate is slower. This causes an accumulation of electrons onto SnO_2, as verified by the transient photocurrent decay measurements. It should be realized that in addition to morphology, the large thickness of SnO_2 sub-layer in the $BiVO_4/Bi_4V_2O_{11}/SnO_2$ film might contribute negatively to the photocurrent. However, the quantitative effect of the film morphology and thickness on the photocurrent could not be estimated in this study.

3.4. Kinetics of charge transfers on the photoanodes

Electrochemical impedance spectroscopy measurements were carried out to evaluate the kinetics of charge transfer in the films. We compared the EIS of a fibrous-like $BiVO_4/Bi_4V_2O_{11}$ and a sponge-like $BiVO_4/Bi_4V_2O_{11}/SnO_2$ films under white light LED ($\lambda > 450$ nm) and dark conditions (Fig. 12) at a potential of 0.7 V (vs. Ag/AgCl). The semicircular feature of the Nyquist diagram (Fig. 12) in the frequency range of 100 kHz–100 mHz is the defining characteristic of the charge transfer process where the diameter of the semicircle is equal to the charge transfer resistance (R_{ct}). The inset shows an equivalent circuit for the photoanodes. Nyquist plot can be interpreted in terms of the equivalent circuit as presented in the inset. In the plot, symbols indicate the experimental data and the lines represent fitting results by using an equivalent circuit. In this work, the EIS data were measured using a three-electrode cell configuration. Consequently, the arc in Nyquist plot indicates the charge transfer kinetics on the working electrode.

In the equivalent Randle circuit, R_s is the solution resistance, Q_1 is the constant phase element for the electrolyte/electrode interface, and R_{ct} is the charge transfer resistance across the interface of electrode/electrolyte. As shown in Fig. 12, the appearance of semicircular features of EIS measurement both in the dark and under illumination was observed, suggesting that charge transfer resistance controls the kinetics at the electrode interface. For both electrodes (fibrous-like $BiVO_4/Bi_4V_2O_{11}$ and sponge-like $BiVO_4/Bi_4V_2O_{11}/SnO_2$), the arc radii under illumination were much smaller than that in the dark, which is due to the increased electron conductivity of the electrodes when irradiated. The fibrous-like $BiVO_4/Bi_4V_2O_{11}$ exhibited a significant decrease in the radius of the arc compared with the sponge-like $BiVO_4/Bi_4V_2O_{11}/SnO_2$ under irradiation, suggesting that the fibrous-like $BiVO_4/Bi_4V_2O_{11}$ surfaces facilitate the transfer of photon-induced holes from the $BiVO_4/Bi_4V_2O_{11}$ to the electrolyte solution. The fitted values of R_{ct} for $BiVO_4/Bi_4V_2O_{11}$ and $BiVO_4/Bi_4V_2O_{11}/SnO_2$ photoanodes were 11218 and 41583 Ω under irradiation respectively, whereas in the dark those R_{ct} values were significantly higher (1.56×10^6 Ω for $BiVO_4/Bi_4V_2O_{11}$, and 7.37×10^6 Ω for $BiVO_4/Bi_4V_2O_{11}/SnO_2$).

3.5. Determination of the PEC efficiency

To determine the overall effectiveness of the photoelectrochemical cells described in this work, we carried out photocurrent-potential measurements in a 2 electrode system, using the prepared photoanodes as a working electrode and Pt wire as a counter electrode, immersed in a 0.5 M Na_2SO_4 solution illuminated by a white light LED ($\lambda > 450$ nm; light intensity: 0.55 mW cm^{-2}). Fig. 13 displays the photocurrent density curves of the $BiVO_4/Bi_4V_2O_{11}$ and $BiVO_4/Bi_4V_2O_{11}/SnO_2$ films in the dark and under light irradiation. The dark current density was negligible at 1.23 V vs. RHE. Under light irradiation, the photocurrent density of fibrous-like $BiVO_4/Bi_4V_2O_{11}$ and sponge-like $BiVO_4/Bi_4V_2O_{11}/SnO_2$ photoanodes was 10 and 7 μA cm^{-2} at 1.23 V vs. RHE, respectively, which indicates that the fibrous-like $BiVO_4/Bi_4V_2O_{11}$ film was approximately 43% more photoactive than sponge-like $BiVO_4/Bi_4V_2O_{11}/SnO_2$ electrode.

The overall efficiency of the photoelectrochemical cells under zero bias conditions was calculated according to equation:

$$\eta_{overall} = \frac{\left(J_{SC}\left(\mathrm{mAcm^{-2}}\right) \times 1.23\mathrm{V} \times \eta_F\right)}{P_{total}\left(\mathrm{mWcm^{-2}}\right)}$$

where J_{SC} is the short-circuit photocurrent density, η_F is the Faradaic efficiency, 1.23 V is the thermodynamic water-splitting potential at 25 °C, and P_{total} is the power density of radiation source. Assuming the Faradaic efficiency as 100%, we found overall efficiencies of 0.14 and 0.11% for the fibrous-like $BiVO_4/Bi_4V_2O_{11}$ and sponge-like $BiVO_4/Bi_4V_2O_{11}/SnO_2$ films, respectively.

4. Conclusions

Two different photoanodes consisting of fibrous-like $BiVO_4/Bi_4V_2O_{11}$ and sponge-like $BiVO_4/Bi_4V_2O_{11}/SnO_2$ were fabricated by spray pyrolysis. The heterojunction formed between $BiVO_4$ and $Bi_4V_2O_{11}$ makes the electrons transfer from the conduction band of $BiVO_4$ to that of $Bi_4V_2O_{11}$ favorable. Nevertheless, the previous deposition of SnO_2 onto FTO led to a decreasing in the photocurrent activity of sponge-like $BiVO_4/Bi_4V_2O_{11}/SnO_2$ compared to that of fibrous-like $BiVO_4/Bi_4V_2O_{11}$ films. Transient photocurrent decay studies confirmed that electrons might accumulate in the semiconductor, thus decreasing its photoactivity. Also, electrochemical impedance studies revealed that the transfer of holes to water occurred more readily in the composite $BiVO_4/Bi_4V_2O_{11}$ than in $BiVO_4/Bi_4V_2O_{11}/SnO_2$ films. Therefore, the overall efficiency for water oxidation in the presence of the fibrous-like $BiVO_4/Bi_4V_2O_{11}$ was higher than that of sponge-like $BiVO_4/Bi_4V_2O_{11}/SnO_2$ films. Moreover, our findings indicated that the preparation of photoelectrodes by spray pyrolysis has a high potential for the design of novel electrodes for photoelectrochemical water splitting.

Acknowledgements

The authors are grateful to CNPq and FAPEMIG—Brazil for the financial support.

References

[1] M. Gratzel, Nature 414 (2001) 338–344.
[2] N.K. Allam, M.A. El-Sayed, J. Phys. Chem. C 114 (2010) 12024–12029.
[3] P. Salvador, Prog. Surf. Sci. 86 (2011) 41–58.
[4] B. Klahr, S. Gimenez, F. Fabregat-Santiago, J. Bisquert, T.W. Hamann, Energy Environ. Sci. 5 (2012) 7626–7636.
[5] S.H. Shen, J. Mater. Res. 29 (2014) 29–46.
[6] C.A. Bignozzi, S. Caramori, V. Cristino, R. Argazzi, L. Meda, A. Tacca, Chem. Soc. Rev. 42 (2013) 2228–2246.
[7] Y. Park, K.J. McDonald, K.S. Choi, Chem. Soc. Rev. 42 (2013) 2321–2337.
[8] A.B. Murphy, P.R.F. Barnes, L.K. Randeniya, I.C. Plumb, I.E. Grey, M.D. Horne, J.A. Glasscock, Int. J. Hydrogen Energy 31 (2006) 1999–2017.
[9] H.W. Jeong, T.H. Jeon, J.S. Jang, W. Choi, H. Park, J. Phys. Chem. C 117 (2013) 9104–9112.
[10] B.A. Pinaud, J.D. Benck, L.C. Seitz, A.J. Forman, Z.B. Chen, T.G. Deutsch, B.D. James, K.N. Baum, G.N. Baum, S. Ardo, H.L. Wang, E. Miller, T.F. Jaramillo, Energ. Environ. Sci. 6 (2013) 1983–2002.
[11] J.K. Cooper, S. Gul, F.M. Toma, L. Chen, Y.S. Liu, J. Guo, J.W. Ager, J. Yano, I.D. Sharp, J. Phys. Chem. C 119 (2015) 2969–2974.
[12] Z.B. Chen, T.F. Jaramillo, T.G. Deutsch, A. Kleiman-Shwarsctein, A.J. Forman, N. Gaillard, R. Garland, K. Takanabe, C. Heske, M. Sunkara, E.W. McFarland, K. Domen, E.L. Miller, J.A. Turner, H.N. Dinh, J. Mater. Res. 25 (2010) 3–16.
[13] J.S. Jang, H.G. Kim, J.S. Lee, Catal. Today 185 (2012) 270–277.
[14] C.X. Kronawitter, L. Vayssieres, S. Shen, L. Guo, D.A. Wheeler, J.Z. Zhang, B.R. Antoun, S.S. Mao, Energy Environ. Sci. 4 (2011) 3889–3899.
[15] K. Trzcinski, A. Borowska-Centkowska, M. Sawczak, A. Lisowska-Oleksiak, Solid State Ion. 271 (2015) 63–68.
[16] Z.S. Liu, J.N. Niu, P.Z. Feng, Y.W. Sui, Y.B. Zhu, RSC Adv. 4 (2014) 43399–43405.

[17] C.M. Ding, J.Y. Shi, D.G. Wang, Z.J. Wang, N. Wang, G.J. Liu, F.Q. Xiong, C. Li, Phys. Chem. Chem. Phys. 15 (2013) 4589–4595.
[18] L. Zhang, E. Reisner, J.J. Baumberg, Energy Environ. Sci. 7 (2014) 1402–1408.
[19] R.v.d. Krol, M. Gratzel, Photoelectrochemical Hydrogen Production, 1 ed., Springer, US, 2012.
[20] N.J. Bell, Y.H. Ng, A. Du, H. Coster, S.C. Smith, R. Amal, J. Phys. Chem. C 115 (2011) 6004–6009.
[21] A. Hagfeldt, H. Lindström, S. Södergren, S.E. Lindquist, J. Electroanal. Chem. 381 (1995) 39–46.
[22] S.J. Hong, S. Lee, J.S. Jang, J.S. Lee, Energ. Environ. Sci. 4 (2011) 1781–1787.
[23] S.U.M. Khan, J. Akikusa, J. Phys. Chem. B 103 (1999) 7184–7189.
[24] J. Premkumar, Chem. Mater. 16 (2004) 3980–3981.
[25] J. Tauc, Amorphous and Liquid Semiconductors, Springer Science & Business Media, 2012.